

# Disentangling Milky Way halo populations at low metallicities using $[\text{Al}/\text{Fe}]^*$

H. Erandes<sup>\*\*1</sup>, Á. Skúladóttir<sup>2</sup>, S. Feltzing<sup>1</sup>, and D. Feuillet<sup>3</sup>

<sup>1</sup> Lund Observatory, Department of Geology, Sölvegatan 12, SE-223 62 Lund, Sweden

<sup>2</sup> Dipartimento di Fisica e Astronomia, Università degli Studi di Firenze, Via G. Sansone 1, I-50019 Sesto Fiorentino, Italy

<sup>3</sup> Observational Astrophysics, Department of Physics and Astronomy, Uppsala University, Box 516, SE-751 20 Uppsala, Sweden

Received XXX; accepted YYY

## ABSTRACT

**Context.** Differentiating between in-situ and accreted populations in the Milky Way halo is a challenging task. Various kinematic spaces are often used to identify distinct accreted populations from the in-situ Milky Way halo. However, this approach has limitations, especially at low orbital energies. To overcome this ambiguity, elemental abundances are typically used to distinguish between the populations. Yet, for many elemental abundance ratios (e.g.  $[\text{Mg}/\text{Fe}]$ ), it remains difficult to make this distinction at low metallicities. Aluminium abundances, on the other hand, have been empirically found to be an effective discriminator, allowing for the separation of accreted and in-situ populations in the Milky Way halo even at low metallicities and low orbital energies.

**Aims.** We aim to test the discriminating power of  $[\text{Al}/\text{Fe}]$  using a well-studied sample of high-velocity stars in the solar vicinity with high-quality spectra. With these stars, we explore the  $[\text{Al}/\text{Fe}]$  ability to separate the in-situ from accreted stars and test its limitations.

**Methods.** We derived aluminium abundances from the Al I 3944 and 3961 Å lines for 45 stars observed in two ESO programmes, along with 11 stars with archival spectra. Aluminium abundances were determined using 1D LTE and 1D NLTE spectral synthesis and line profile fitting.

**Results.** We confirm that the low- $\alpha$  population (associated with accreted stars) systematically has lower  $[\text{Al}/\text{Fe}]$  compared to high- $\alpha$  (in situ) stars. However, at low  $[\text{Fe}/\text{H}] \approx -1.4$  we identify three stars, previously categorised as in-situ or thick-disk stars as having low  $[\text{Al}/\text{Fe}] < -0.3$ , indicating that they might actually be accreted.

**Conclusions.** Aluminium abundances, when carefully measured and NLTE effects taken into account, are effective tracers of the chemical history of halo stars. They provide an independent constraint on origin, complementing  $\alpha$ -element abundances trends, and help us to disentangle subpopulations within the accreted halo, especially in the metal-poor regime.

**Key words.** Galaxy: halo, Galaxy: abundances, abundances – stars: abundances — galaxies: evolution — galaxies: individual: *Gaia*-Sausage-Enceladus, nuclear reactions, nucleosynthesis

## 1. Introduction

The stellar halo of the Milky Way preserves the signatures of its hierarchical assembly. Early studies revealed that the Galactic halo is not chemically homogeneous, but instead contains stars with distinct enrichment histories. By studying halo stars passing through the solar neighbourhood, Nissen & Schuster (2010) discovered that they divide into two chemically distinct groups, a high- $\alpha$  and a low- $\alpha$  population. With the advent of *Gaia*, it has become clear that the Galactic halo shows evidence of multiple accretion events, the largest of which is the *Gaia*-Sausage-Enceladus (Abbott et al. 2017; Belokurov et al. 2018). The low- $\alpha$  population identified by Nissen & Schuster has since been shown to largely correspond to this accreted dwarf galaxy (Skúladóttir et al. 2025).

There are different ways to disentangle accreted stars from the in-situ halo population. One option is kinematic selection, which uses orbital actions and their angular momenta to isolate

the debris from the in-situ components (e.g. Feuillet et al. 2020). However, purely kinematic criteria vary in completeness and purity depending on the adopted potential and selection method (Carrillo et al. 2024; Feltzing & Feuillet 2023; Erandes et al. 2024). Another approach is chemical selection together with kinematics, in which elemental abundances are used to distinguish populations (e.g. Limberg et al. 2022; Buder et al. 2021; Naidu et al. 2022). In this context, aluminium abundances have recently emerged as a particularly powerful tool. Empirical studies have shown that accreted stars, and stars in dwarf galaxies, display systematically lower  $[\text{Al}/\text{Fe}]$  compared to in-situ stars at the same metallicity (Hawkins et al. 2015; Hasselquist et al. 2021; Feuillet et al. 2022). Moreover, aluminium abundances have been demonstrated to separate not only in-situ from accreted halo stars, but also different subpopulations within the accreted component (Skúladóttir et al. 2025).

The nucleosynthetic origin of aluminium helps explain its discriminating power. Aluminium is primarily produced in massive stars during hydrostatic carbon burning, with an additional contribution from neon burning (Woosley & Weaver 1995). Under these conditions, it can behave as a primary element, showing little dependence on metallicity. However, secondary production channels, involving  $\alpha$ -, n-, and p-capture reactions on neutron-rich seed nuclei such as  $^{22}\text{Ne}$  and  $^{23}\text{Na}$ , also contribute

\* Based on observations collected at the European Southern Observatory under ESO programme IDs 109.22 and 110.240 (PI: Á. Skúladóttir) as well as obtained from the ESO Science Archive Facility under the ESO programme 8.B-0475, 076.B-0133, 090.B-0605, 109.23, 71.B-0529, and 68.D-0094

\*\* e-mail: heitor.ernandes@geol.lu.se

(Roederer & Lawler 2021a). As a result, aluminium can exhibit metallicity-dependent behaviour. Indeed, Kobayashi et al. (2020) point out that in the Milky Way, aluminium follows trends characteristic of a secondary element. Importantly, the relative efficiency of these processes depends on the initial mass function, star formation history, and chemical enrichment timescales, which differ between the Milky Way and its satellites. This dependence of the efficiency of aluminium production on various parameters of galaxy evolution explains why aluminium abundances can vary systematically between accreted and in-situ populations.

The Nissen & Schuster sample provides an ideal dataset to test the ability of aluminium to distinguish halo populations. The stars were selected to have large space velocities ( $V_{\text{total}} > 180 \text{ km s}^{-1}$ ) relative to the local standard of rest, ensuring a high probability of belonging to the halo. Additional selection criteria used the Strömgen indices to select dwarfs and subgiants with  $5200 \text{ K} < T_{\text{eff}} < 6300 \text{ K}$  and  $[\text{Fe}/\text{H}] > -1.6$ , to reduce parameter-dependent systematic effects. Because of this narrow parameter range, NLTE corrections are expected to be relatively uniform across the sample. The original discovery of the high- and low- $\alpha$  sequences was based on this dataset, and it has since become a benchmark for studies of the Galactic halo.

An important feature of the Nissen & Schuster sample is that it provides small-number statistics with very high precision (Lindgren & Feltzing 2013). This means that, while the dataset is modest in size, it offers some of the most accurate stellar parameters and elemental abundances available. Until recently, aluminium abundance could not be derived for these metal-poor stars due to the lack of observations of the near-UV lines. With new observations in addition to archival UVES spectra covering the bluer wavelength region, it is now possible to measure aluminium using its resonance lines, at 3944 and 3961 Å, in this key sample for the first time.

The aim of this work is to test the capability of aluminium abundances in separating in-situ from accreted halo stars, using the Nissen & Schuster sample as a benchmark. We explored the potential of aluminium as a tracer of substructure within the accreted halo in Skúladóttir et al. (2025), and discuss both its discriminating power and its limitations.

## 2. Observations, archival data, and data reductions

### 2.1. Target selection and data reduction

The stellar sample analysed in this work is a subsample of the 66 stars studied by Nissen & Schuster (2010, 2011); Nissen et al. (2024). From this larger set, we selected those that could be observed in the Southern hemisphere with VLT/UVES (Dekker et al. 2000).

New spectra were obtained for 45 stars with the blue arm of UVES. These data were collected in two ESO programmes (PI: Á. Skúladóttir, ESO ID 109.22 and 110.240). The observations were carried out at high spectral resolution ( $R > 40,000$ ) and achieved a signal-to-noise ratio above 150 per pixel. We used the UVES 390 setting, which covers the wavelength range 3260–4540 Å<sup>1</sup>.

In addition to the new observations, we included 11 stars with suitable archival UVES spectra. These data also cover the region of the Al I lines (3900–4000 Å) with similarly high signal-to-noise ratios ( $\text{SNR} > 150 \text{ pix}^{-1}$ ). The archival material comes

from ESO programmes 68.B-0475, 076.B-0133, 090.B-0605, 109.23, 71.B-0529, and 68.D-0094.

Both the new and archival spectra were reduced using the standard UVES pipelines (Freudling et al. 2013). Most stars were observed with the UVES 390 setting, but three stars, G188-22, HD 25704, and G53-41, were observed with the 437 setting, which covers 3730–4990 Å and therefore includes the Al I lines.

### 2.2. Radial velocity

After the data reduction and application of the wavelength solution, all spectra were corrected for their heliocentric velocity. This step ensures that the observed wavelengths are placed in the rest frame of the Sun, allowing for consistent comparison between the observations.

Radial velocities were determined using a minimisation procedure in which synthetic spectra, computed with TURBOSPECTRUM (Alvarez & Plez 1998; Plez 2012), were fitted to the observations. The stellar parameters adopted for the synthetic spectra were taken from Nissen et al. (2024). By comparing each observed spectrum to the corresponding synthetic template, we identified the velocity shift that minimised the residuals, thus providing a robust measurement of the stellar radial velocity.

For each star, the median radial velocity derived from all available observations is reported in Table A.1. This approach reduces the impact of noise or possible systematics in individual exposures. We note that the star HD 111980 is a single-lined spectroscopic binary (SB1), and its radial velocity variability is therefore intrinsic to its binary nature.

### 2.3. Co-addition and Normalization

After applying the radial velocity correction to each exposure, we co-added the spectra for each star by summing the unnormalised flux across the UVES blue and red arms (for the settings: 390, 437, 554l, and 564u). This procedure preserves the flux information and ensures that the signal-to-noise ratio in each region is maximised. Some stars were observed up to nine times (see Table A.1), whereas the majority have only a single exposure. In this work, we focus on the 390 and 437 settings, which were used to derive the aluminium abundances.

The normalisation of the spectra was performed using a method based on continuum points determined from a synthetic spectrum template created using TURBOSPECTRUM. Because this approach incorporates information about line positions and broadening, it provides a reliable identification of the true continuum. A three-step procedure was implemented in order to mitigate observational artefacts such as telluric absorption, cosmic rays, and residual signatures of the blaze function in individual echelle orders. In the first step, a renormalisation placed the synthetic and observed spectra on the same overall scale while preserving their shapes. The second step identified continuum points in the observed spectra based on the locations predicted by the synthetic template. Finally, a third pass re-evaluated the continuum points in the processed observations and refined the continuum placement.

For the 390 setting, this procedure was applied separately in three spectral regions in order to account for the challenges posed by the near-UV, particularly around the Balmer jump. A template atmosphere with parameters  $T_{\text{eff}} = 5900 \text{ K}$ ,  $\log g = 4.2$ ,  $[\text{Fe}/\text{H}] = -1.0$ , and  $v_{\text{mic}} = 1.0 \text{ km s}^{-1}$  was used to identify candidate continuum points. Points above a threshold flux of 0.99 were retained, and their analogues in the observed spectra were

<sup>1</sup> <https://www.eso.org/sci/facilities/paranal/instruments/uves/doc.html>

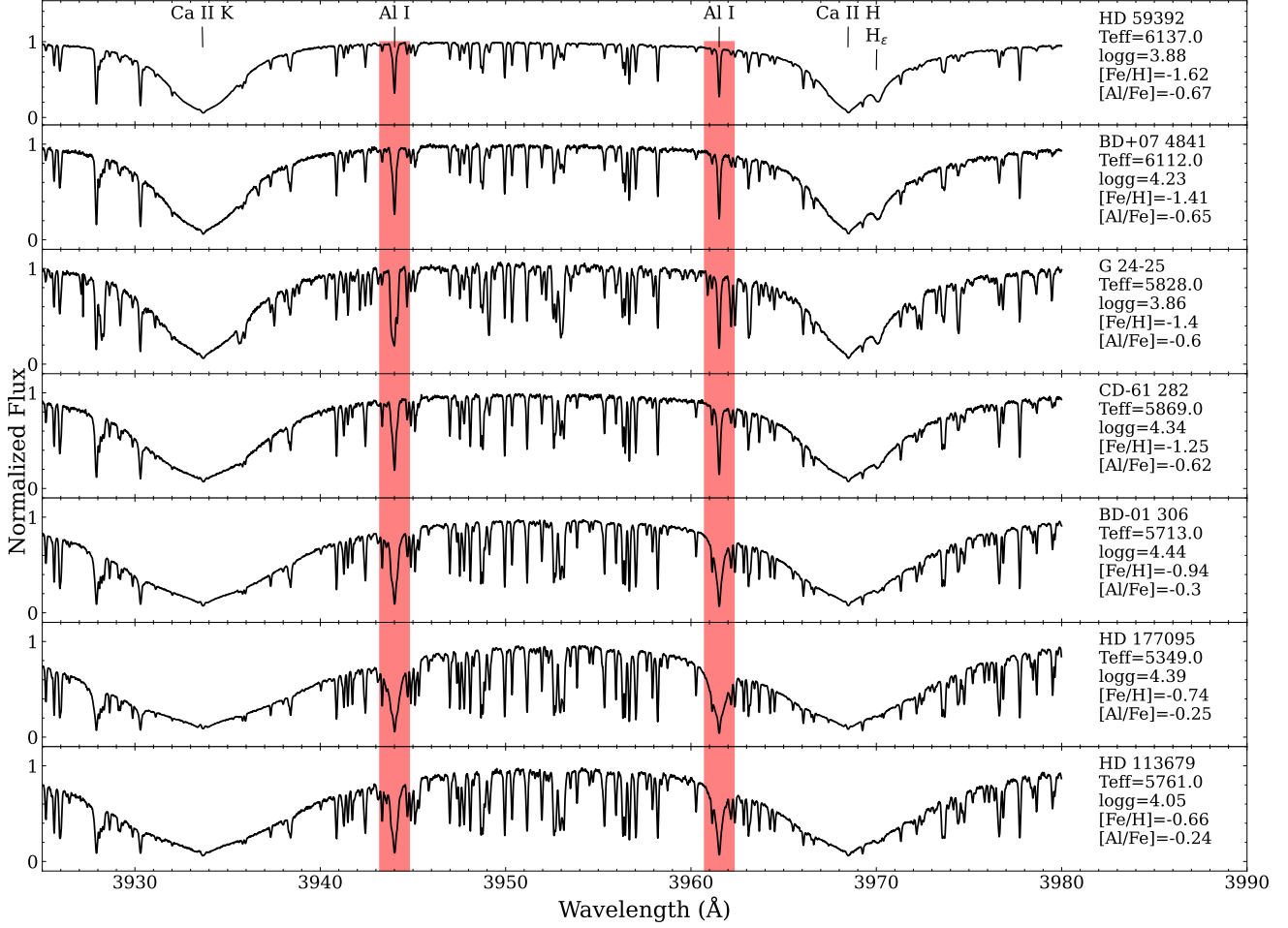


**Fig. 1.** Normalised spectra for seven stars spanning a range of metallicities, from  $[\text{Fe}/\text{H}] = -1.41$  at the top to  $[\text{Fe}/\text{H}] = -0.66$  in the bottom panel. The Al I 3944 and 3961 Å lines used to derive Al abundance are highlighted in red. We also indicate the position of the Ca II H & K lines and  $H_{\epsilon}$ .

fitted with a third-order Chebyshev polynomial. After the first normalisation, this procedure was repeated on the observed spectra, selecting only continuum points that were both above the threshold and present in the initial set. A final polynomial fit was then adopted as the continuum. The same approach was applied to the 437, 564u, and 564l settings, without the need for splitting into multiple regions. The 564u, and 564l settings will be analysed in Shejeelammal et al. in prep.

Examples of the resulting spectra are shown in Fig. 1. These illustrate the particular difficulties of continuum placement in the near-UV, where the Ca II H and K lines dominate the spectral region. The challenge becomes especially pronounced at higher metallicities, where line crowding is severe (bottom spectra in Fig. 1).

### 3. Atomic Data

The atomic data used in the elemental abundance analysis are provided in Table 1, including references for the energy levels and the  $\log(gf)$ . We used VALD as a source of the Hyperfine structures (hfs)<sup>2</sup> Where the original sources for the hyperfine structures are Barklem et al. (2000); Smith & Liszt (1971); Brown & Evenson (1999); Zhan-Kui et al. (1982).

<sup>2</sup> <https://vald.astro.uu.se/>

## 4. Determination of aluminium abundances

### 4.1. Stellar atmospheric parameters

Stellar parameters for the majority of our sample were adopted from Nissen et al. (2024). For stars not included in that work, we used the parameters reported by Nissen & Schuster (2011), as indicated by the NSflag in Table 2. For a subset of stars, 3D  $[\text{Fe}/\text{H}]$  values are available from Amarsi et al. (2019, 2022); Nissen et al. (2024). The difference between the 1D and 3D  $[\text{Fe}/\text{H}]$  is small, with an average offset of only 0.02 dex across our sample.

For the sake of homogeneity in the abundance analysis, we adopted the 1D  $[\text{Fe}/\text{H}]$  values from Nissen & Schuster (2011) when computing the synthetic spectra. This choice ensures consistency across the full dataset, as not all stars had 3D metallicities available.

### 4.2. Aluminum abundances derived from the Al I 3944 and 3961 Å lines

The aluminium abundances were derived from the resonance lines at 3944 and 3961 Å. Both lines are located in the wings of the strong Ca II H and K features, in a spectral region that is heavily crowded with absorption lines, including the Balmer- $\epsilon$  ( $H_{\epsilon}$ ) line, see Fig. 1. Because of this, we fitted the aluminium

**Table 1.** Atomic data for the Al I and Ca II lines analysed in this paper. The wavelength, excitation potential ( $\chi_{ex}$ ), and  $\log(gf)$  values for each line, as well as the energy levels and term configurations of the lower and upper states, are listed. Hyperfine structure components for the Al I lines were adopted from sources found in a search in VALD. References for the atomic data are provided in the final column.

Species	Wavelength [Å]	$\chi_{ex}$ [eV]	$\log(gf)$	Lower Level		J	Upper Level		J	Reference
				Energy [cm <sup>-1</sup> ]	ConFig.		Energy [cm <sup>-1</sup> ]	ConFig.		
Al I	3944.01	0.000	-0.623	0.000	3s <sup>2</sup> 3p <sup>2</sup> P <sup>o</sup>	1/2	25347.756	3s <sup>2</sup> 4s <sup>2</sup> S	1/2	Eriksson & Isberg (1963)
Al I	3961.52	0.014	-0.333	112.061	3s <sup>2</sup> 3p <sup>2</sup> P <sup>o</sup>	3/2	25347.756	3s <sup>2</sup> 4s <sup>2</sup> S	1/2	Eriksson & Isberg (1963)
Ca II	3933.66	5.884	0.135	0.000	3p <sup>6</sup> 4s <sup>2</sup> S	1/2	25414.40	3s <sup>6</sup> 4p <sup>2</sup> P <sup>o</sup>	3/2	Edlén & Risberg (1956)
Ca II	3968.47	4.131	-0.18	0.000	3p <sup>6</sup> 4s <sup>2</sup> S	1/2	25191.51	3p <sup>6</sup> 4p <sup>2</sup> S	1/2	Edlén & Risberg (1956)

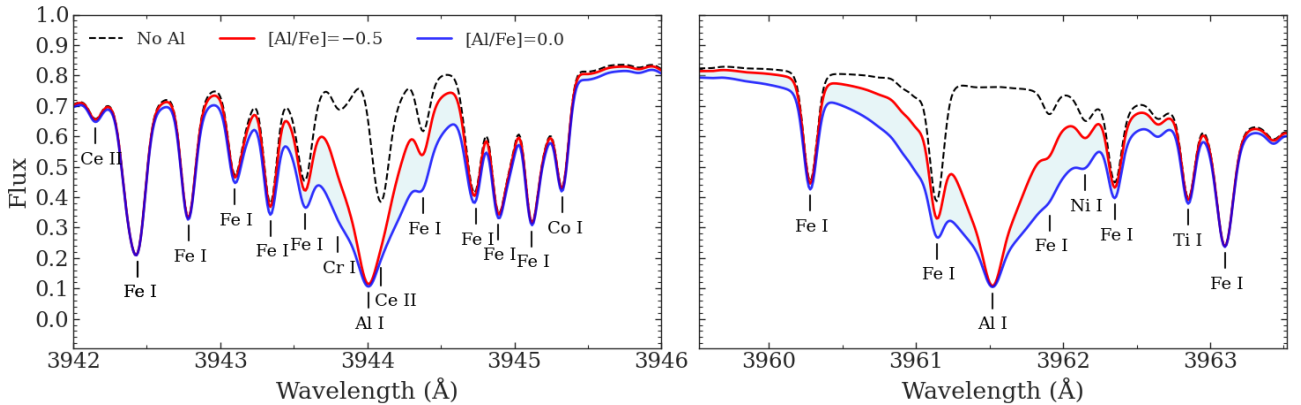


**Fig. 2.** Synthetic NLTE spectra showing the shape of the Aluminium lines 3944 Å and 3961 Å and their blends as indicated. For the synthetic spectra, the star HD 177095 at  $[\text{Fe}/\text{H}] = -0.74$  serves as an example for the NLTE calculations. Dashed lines indicate a spectrum with no aluminium present, while the red and blue lines show spectra with  $[\text{Al}/\text{Fe}] = -0.5$  and  $0.0$  respectively.

lines individually using a non-automated approach, carefully reproducing their unique blend patterns as shown in Fig. 2.

The 3961 Å line is the least blended of the two lines, see Fig. 2. Therefore adopted as the primary abundance indicator. Its main contamination arises from nearby Fe II lines. In contrast, the 3944 Å line is affected by several blends: a Ce II line on the red wing, a Cr II line on the blue wing, and additional Fe II lines. For this reason, abundances derived from the 3944 Å line are less reliable, although they were used to cross-check the results.

Previous studies have shown that NLTE effects significantly impact the formation of the Al I lines. In particular, Nordlander & Lind (2017) demonstrated that for dwarf stars with metallicities in the range  $-1.0 < [\text{Fe}/\text{H}] < -0.5$ , the NLTE correction for the 3961 Å line is typically around +0.2 dex in  $[\text{Al}/\text{Fe}]$  (see also Koutsouridou et al. 2025). These findings are supported by the empirical analysis of Roederer & Lawler (2021b). Following these results, we performed the abundance analysis in NLTE, in addition to LTE.

Synthetic spectra were computed with TURBOSPECTRUM (Alvarez & Plez 1998; Plez 2012; Gerber et al. 2023), which allows a straightforward switch between LTE and NLTE calculations. For the NLTE analysis, we employed the grids provided by Ezzeddine et al. (2018). Our fitting procedure first determined the broadening and the calcium abundance that best reproduced the Ca II H and K wings, as these strongly influence the local continuum. The aluminium abundance was then derived by fitting the 3961 Å line through  $\chi^2$  minimisation, ensuring that both the line core and the extended wings were simultaneously reproduced. Finally, the abundance inferred from the 3944 Å line was checked for consistency. Examples of the line profile, to-

gether with indications of the most prominent blending features, are shown in Fig. 2.

The NLTE analysis also provides an improved reproduction of the aluminium line profiles. In particular, the characteristic wing shape of the 3961 Å feature is better matched under NLTE, supporting the reliability of the derived abundances. The typical NLTE correction for the 3961 Å line is approximately +0.2 dex, consistent with the predictions of Nordlander & Lind (2017) and the empirical findings of Roederer & Lawler (2021b). Figure B.1 illustrates these corrections as a function of stellar parameters, confirming that the magnitude of the effect depends mildly on effective temperature but is largely insensitive to surface gravity.

## 5. Uncertainties in the resulting abundance

The uncertainties in the derived aluminium abundances arise primarily from the uncertainties in the adopted stellar parameters. To estimate these effects, we followed the methodology of Erandes et al. (2020), Bensby et al. (2004), and Epstein et al. (2010), in which the atmospheric parameters are varied individually and the corresponding changes in the best-fit aluminium abundance are measured.

For this sample, we adopted the typical parameter uncertainties reported by Nissen & Schuster (2010):  $\Delta T_{\text{eff}} = 50$  K,  $\Delta \log g = 0.10$  dex,  $\Delta v_{\text{mic}} = 0.10$  km s<sup>-1</sup>, and  $\Delta [\text{Fe}/\text{H}] = 0.05$  dex. Applying these variations to the 3961 Å line, we find abundance sensitivities of (+0.05, -0.03, 0.00, -0.07) dex for changes in  $T_{\text{eff}}$ ,  $\log g$ ,  $v_{\text{mic}}$ , and  $[\text{Fe}/\text{H}]$ , respectively.

The total uncertainty was obtained by summing these contributions in quadrature, yielding a typical error of 0.09 dex in

**Table 2.** Stellar parameters for the stars analysed in this work. Effective temperature ( $T_{\text{eff}}$ ), surface gravity ( $\log g$ ), microturbulence ( $v_{\text{mic}}$ ), and [Fe/H], 1D and 3D for each star, along with their original classification (high- $\alpha$ , low- $\alpha$ , or thick-disk) and the source of the stellar parameters, as “NSflag” with “NS24” for Nissen et al. (2024) and “NS11” for Nissen & Schuster (2011). In the last column, the new classification based on the Aluminium elemental abundance in the current paper is presented.

Star-ID	<i>Gaia</i> DR3 ID	N24-ID	$T_{\text{eff}}$ [K]	$\log g$	$v_{\text{mic}}$ [km s <sup>-1</sup> ]	[Fe/H]		NSflag	NS Class	Al Class
						1D	3D			
BD+00 2058A	3085891537839267328	G 112-43	6209	4.02	1.17	-1.27	-1.28	NS24	low- $\alpha$	low-Al
BD+02 2541	3700341138433848832	G 13-38	5263	4.54	0.90	-0.88	—	NS11	high- $\alpha$	high-Al
BD+06 2932	1159108770069883136	G 66-22	5297	4.46	0.78	-0.88	-0.90	NS24	low- $\alpha$	low-Al
BD+07 4841	2722849325377392384	G 18-39	6112	4.23	1.44	-1.41	-1.39	NS24	high- $\alpha$	low-Al
BD+11 2369	3916257626962267136	G 57-07	5755	4.33	0.99	-0.48	-0.51	NS24	high- $\alpha$	high-Al
BD+11 4725	2728314787225296000	G 18-28	5443	4.49	0.88	-0.85	-0.86	NS24	high- $\alpha$	high-Al
BD+18 3423	4550762289589343488	G 170-56	6112	4.11	1.39	-0.94	-0.93	NS24	low- $\alpha$	low-Al
BD-01 306	2494759795723713408	G 159-50	5713	4.44	1.03	-0.94	-0.96	NS24	high- $\alpha$	high-Al
BD-03 56	2540830947835865728	G 31-55	5731	4.35	1.26	-1.12	-1.12	NS24	high- $\alpha$	high-Al
BD-06 855	3202470247468181632	G 82-05	5338	4.51	0.80	-0.78	-0.81	NS24	low- $\alpha$	low-Al
BD-08 4501	4165370682239910144	G 20-15	6162	4.32	1.50	-1.5	-1.49	NS24	low- $\alpha$	low-Al
CD-33 3337	5579891291853909504	CD-33 3337	6112	3.86	1.56	-1.37	-1.37	NS24	TD	low-Al
CD-43 6810	5388634989413677440	CD-43 6810	6059	4.32	1.24	-0.44	-0.44	NS24	high- $\alpha$	high-Al
CD-57 1633	5486881507314450816	CD-57 1633	5981	4.29	1.08	-0.91	-0.93	NS24	low- $\alpha$	low-Al
G 24-25	4228176122142169600	G 24-25	5828	3.86	1.20	-1.40	—	NS11	high- $\alpha$	low-Al
G 63-26	3939515154043771392	G 63-26	6175	4.17	1.65	-1.58	-1.58	NS24	high- $\alpha$	—
G 75-31	2502689198705422848	G 75-31	6135	4.02	1.28	-1.04	-1.05	NS24	low- $\alpha$	low-Al
HD 103723	3494135429225414016	HD 103723	6050	4.20	1.11	-0.81	-0.82	NS24	low- $\alpha$	low-Al
HD 105004	3486853672952159872	HD 105004	5852	4.35	1.09	-0.83	-0.84	NS24	low- $\alpha$	low-Al
HD 106516	3581001280225616128	HD 106516	6327	4.43	1.18	-0.69	-0.71	NS24	TD	high-Al
HD 111980	3510294882898890880	HD 111980	5878	3.98	1.39	-1.09	-1.08	NS24	high- $\alpha$	high-Al
HD 113679	6141991322784963072	HD 113679	5761	4.05	1.37	-0.66	-0.65	NS24	high- $\alpha$	high-Al
HD 120559	5871764831114179968	HD 120559	5486	4.58	1.05	-0.91	-0.90	NS24	TD	high-Al
HD 121004	6095425184286680064	HD 121004	5755	4.43	1.16	-0.71	-0.70	NS24	high- $\alpha$	high-Al
HD 132475	6232043867720079616	HD 132475	5750	3.77	1.37	-1.51	-1.51	NS24	high- $\alpha$	high-Al
HD 148816	4433711099194059904	HD 148816	5923	4.17	1.33	-0.74	-0.74	NS24	high- $\alpha$	high-Al
HD 159482	4485972467412021376	HD 159482	5829	4.37	1.21	-0.74	-0.73	NS24	high- $\alpha$	high-Al
HD 163810	4150413750729448320	HD 163810	5592	4.61	1.17	-1.22	-1.19	NS24	low- $\alpha$	low-Al
HD 177095	4082356695359119616	HD 177095	5349	4.39	0.90	-0.74	—	NS11	high- $\alpha$	high-Al
HD 179626	4263841431819084032	HD 179626	5925	4.14	1.49	-1.06	-1.04	NS24	high- $\alpha$	high-Al
HD 189558	4189078626829509248	HD 189558	5707	3.83	1.29	-1.14	-1.13	NS24	TD	high-Al
HD 193901	6859076107589173120	HD 193901	5729	4.43	1.31	-1.11	-1.08	NS24	low- $\alpha$	low-Al
HD 194598	1752459532807704704	HD 194598	6018	4.34	1.40	-1.11	-1.08	NS24	low- $\alpha$	low-Al
HD 199289	6481426917515214464	HD 199289	5915	4.30	1.21	-1.05	-1.04	NS24	TD	high-Al
HD 205650	6810862213470371072	HD 205650	5793	4.35	1.17	-1.19	-1.17	NS24	TD	high-Al
HD 219617	4263841431819084032	HD 219617	5983	4.28	1.42	-1.46	-1.44	NS24	high- $\alpha$	high-Al
HD 22879	3250489115709122560	HD 22879	5859	4.29	1.20	-0.86	-0.85	NS24	TD	high-Al
HD 284248	52624073910834176	HD 284248	6271	4.21	1.51	-1.59	-1.59	NS24	low- $\alpha$	low-Al
HD 298986	5358179685572496384	CD-51 4628	6296	4.29	1.31	-1.32	-1.34	NS24	low- $\alpha$	low-Al
HD 3567	2427069874188580480	HD 3567	6180	4.01	1.40	-1.17	-1.18	NS24	low- $\alpha$	low-Al
HD 51754	3112836479029139200	HD 51754	5857	4.35	1.30	-0.58	-0.57	NS24	high- $\alpha$	high-Al
HD 59392	5586241315104190848	HD 59392	6137	3.88	1.73	-1.62	-1.62	NS24	low- $\alpha$	low-Al
HD 76932	5730371484020807808	HD 76932	5977	4.17	1.30	-0.87	-0.87	NS24	TD	high-Al
Wolf 615	4412702764879270656	G 16-20	5625	3.64	1.50	-1.42	—	NS11	low- $\alpha$	low-Al
CD-61 282	4715919175280799616	CD-61 282	5869	4.34	1.19	-1.25	-1.23	NS24	—	low-Al
Archival spectra										
CD-45 3283	5510893810476230144	CD-45 3283	5685	4.61	0.95	-0.93	-0.93	NS24	low- $\alpha$	—
G 46-31	3845429561802456704	G 46-31	6017	4.29	1.30	-0.83	-0.82	NS24	low- $\alpha$	—
G 87-13	940306024863622400	G 87-13	6217	4.11	1.42	-1.11	-1.09	NS24	low- $\alpha$	low-Al
G 98-53	3440045641893430912	G 98-53	5954	4.26	1.20	-0.89	-0.87	NS24	low- $\alpha$	low-Al
G 114-42	5759671677898613632	G 114-42	5721	4.40	1.19	-1.12	-1.10	NS24	low- $\alpha$	low-Al
G 161-73	3822808140853060224	G 161-73	6108	3.99	1.26	-1.01	-1.04	NS24	low- $\alpha$	low-Al
G 53-41	3855475490307708032	G 53-41	5956	4.34	1.35	-1.21	-1.16	NS24	low- $\alpha$	—
G 119-64	761871677268717952	G 119-64	6333	4.14	1.40	-1.50	-1.52	NS24	low- $\alpha$	low-Al
G 05-36	68752844338431488	G 05-36	6139	4.22	1.29	-1.25	-1.24	NS24	high- $\alpha$	high-Al
G 188-22	1800518563283501440	G 188-22	6116	4.20	1.42	-1.33	-1.32	NS24	high- $\alpha$	high-Al
HD 25704	4682867168555426944	HD 25704	5974	4.30	1.30	-0.86	-0.85	NS24	TD	high-Al

[Al/Fe] for the 3961 Å line. This value represents the dominant source of random uncertainty in our measurements.

Additional uncertainties may arise from continuum placement and line blending, especially in the case of the 3944 Å line. However, as the 3961 Å line was adopted as our primary abun-

dance indicator, these effects have a minimal impact on our final results, given the high quality of our data.

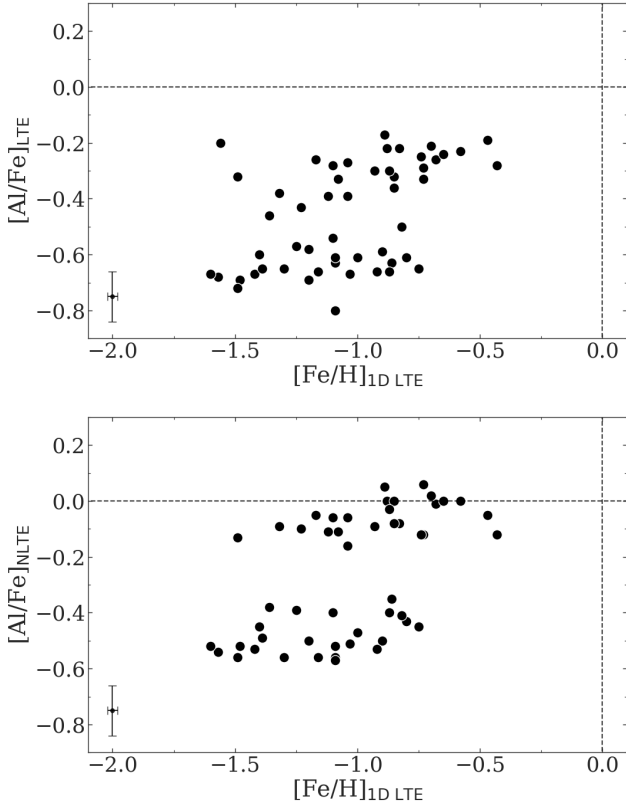


**Fig. 3.**  $[\text{Al}/\text{Fe}]$  as a function of  $[\text{Fe}/\text{H}]$  for the full stellar sample in LTE in the upper panel and NLTE in the lower panel. The abundances are derived from the Al I 3961 Å line.

## 6. Results

### 6.1. $[\text{Al}/\text{Fe}]$ vs. $[\text{Fe}/\text{H}]$ trends

Aluminium abundances were measured from both the 3944 and 3961 Å lines, and the results are listed in Table 3. Figure 3 shows  $[\text{Al}/\text{Fe}]$  as a function of  $[\text{Fe}/\text{H}]$  for the full stellar sample. The upper panel presents the LTE abundances, while the lower panel displays the abundances corrected for NLTE effects. In both cases, the results separate into two groups of low- and high-Al abundances.

The separation between the two groups is already visible in LTE, but the distinction becomes sharper in NLTE, demonstrating the importance of applying NLTE corrections when studying aluminium in metal-poor halo stars. A 3D NLTE analysis can change the shape of the Al I line near the core as shown in Fig. 3 in Nordlander & Lind (2017) paper. However, it is also discussed there that both 1D and 3D models reproduce well the line shape as soon as the calcium abundance is derived to set the continuum.

## 7. Discussion

In this section, we discuss whether aluminium abundances can serve as a reliable discriminator between in-situ and accreted halo populations, and evaluate the strengths and limitations of this approach. Our analysis shows that the division between high- and low-aluminium stars is robust across the full metallicity range, and that NLTE corrections enhance the clarity of this separation. Below, we discuss the implications of this result in terms of population classification, nucleosynthesis, kinematic

**Table 3.** Aluminium and calcium abundances for the sample stars. The table lists the  $[\text{Al}/\text{Fe}]$  abundances derived from the 3944 Å and 3961 Å Al I lines, along with NLTE corrections for the 3961 Å line ( $\Delta[\text{Al}/\text{Fe}]_{\text{NLTE}}$ ). Also shown are the  $[\text{Ca}/\text{Fe}]$  values derived from the Ca II H and K lines.

Star-id	$[\text{Al}/\text{Fe}]_{\text{LTE}}$		$\Delta[\text{Al}/\text{Fe}]_{\text{NLTE}}$	$[\text{Ca}/\text{Fe}]_{\text{LTE}}$
	3944 Å	3961 Å	3961 Å	
BD+00 2058A	-0.55	-0.57	0.18	0.29
BD+02 2541	—	-0.22	0.22	-0.22
BD+06 2932	-0.58	-0.63	0.28	-0.15
BD+07 4841	-0.66	-0.65	0.16	0.24
BD+11 2369	-0.15	-0.19	0.14	-0.12
BD+11 4725	-0.19	-0.22	0.14	-0.12
BD+18 3423	-0.66	-0.66	0.13	0.10
BD-01 306	-0.25	-0.30	0.21	0.00
BD-03 56	-0.28	-0.28	0.22	0.05
BD-06 855	-0.61	-0.65	0.20	-0.16
BD-08 4501	-0.72	-0.72	0.16	0.29
CD-33-3337	-0.50	-0.46	0.08	0.33
CD-43 6810	-0.28	-0.28	0.16	-0.10
CD-57 1633	-0.55	-0.59	0.09	0.00
G 24-25	—	-0.60	0.15	0.00
G 63-26	-0.24	-0.20	—	0.36
G 75-31	-0.65	-0.67	0.16	0.15
HD 103723	-0.54	-0.61	0.18	0.07
HD 105004	-0.52	-0.50	0.09	0.05
HD 106516	-0.30	-0.26	0.25	0.07
HD 111980	-0.28	-0.33	0.22	0.15
HD 113679	-0.21	-0.24	0.24	0.00
HD 120559	-0.17	-0.17	0.22	-0.11
HD 121004	-0.17	-0.21	0.23	-0.02
HD 132475	-0.28	-0.32	0.19	0.19
HD 148816	-0.33	-0.33	0.21	-0.05
HD 159482	-0.29	-0.29	0.35	0.12
HD 163810	-0.64	-0.69	0.19	-0.08
HD 177095	-0.25	-0.25	0.13	-0.19
HD 179626	-0.39	-0.39	0.23	0.04
HD 189558	-0.39	-0.39	0.28	0.12
HD 193901	-0.76	-0.80	0.23	0.00
HD 194598	-0.60	-0.61	0.09	0.10
HD 199289	-0.21	-0.27	0.21	0.07
HD 205650	—	-0.26	0.21	0.05
HD 219617	-0.60	-0.57	0.23	0.24
HD 22879	-0.32	-0.36	0.28	0.00
HD 284248	-0.68	-0.68	0.14	0.34
HD 298986	-0.65	-0.65	0.09	0.26
HD 3567	-0.65	-0.66	0.10	0.20
HD 51754	-0.18	-0.23	0.23	-0.09
HD 59392	-0.60	-0.67	0.15	0.37
HD 76932	-0.22	-0.30	0.27	0.09
Wolf 615	-0.62	-0.67	0.14	0.07
CD-61 282	-0.60	-0.62	0.17	0.10
Archival spectra				
CD-45 3283	-0.71	-0.71	—	-0.10
G 46-31	—	—	—	0.00
G 87-13	-0.63	-0.63	0.07	0.16
G 98-53	-0.68	-0.66	0.26	0.04
G 114-42	-0.52	-0.54	0.14	0.04
G 161-73	-0.62	-0.61	0.14	0.11
G 53-41	-0.58	-0.58	—	0.16
G 119-64	-0.69	-0.69	0.17	0.31
G 05-36	-0.45	-0.43	0.33	0.33
G 188-22	-0.36	-0.38	0.29	0.31
HD 25704	-0.30	-0.32	0.32	0.03

selections, and its relation to the Nissen & Schuster classification.



### 7.1. High-Aluminum and Low-Aluminium

In Fig. 4 (upper panel) we present our classification of the sample into high- and low-aluminium stars, adopting NLTE abundances from the Al I 3961 Å line.

A clear division emerges at  $[Al/Fe] = -0.3$ , which we adopt as the threshold separating high- and low-aluminium stars. This boundary effectively distinguishes stars with systematically enhanced aluminium abundances predominantly associated with the in-situ halo and thick disk from those with depleted values, which trace the accreted population. The lower panel places this division in the  $[\alpha/Fe]$  context, showing  $[Mg/Fe]$  as a function of  $[Fe/H]$ . Here, the high-Al stars overlap closely with the high- $\alpha$  sequence, while the low-Al stars coincide with the low- $\alpha$  sequence. In particular, at high  $[Fe/H] > -1.3$ , the low- $\alpha$  and low-Al populations are identical. However, at low  $[Fe/H] < -1.3$  we notice two low-Al stars previously categorised as high- $\alpha$  (red diamonds) and one as a thick disk star (red cross). Notably, the separation of the two populations in  $[\alpha/Fe]$  diminishes at low  $[Fe/H]$  (where both  $\alpha$ -elements and Fe mainly come from core-collapse supernovae). On the other hand, the separation in  $[Al/Fe]$  stays clear, underscoring the discriminating power of aluminium as a powerful tracer of accreted stars in the halo, especially at low  $[Fe/H]$ .

This classification not only provides a clean division in chemical abundance space but also offers an important advantage for disentangling halo populations whose kinematic signatures alone may be ambiguous, especially at lower energies. Aluminium can be a complementary tracer to  $\alpha$ -elements for chemical tagging of halo stars. However, as discussed below, the interpretation of aluminium abundances must be tempered by an understanding of their nucleosynthetic origin and limitations.

### 7.2. Al nucleosynthesis and limitations

Aluminium is produced in massive stars through hydrostatic carbon and neon burning (Woosley & Weaver 1995). It can act as a primary element, but also as a secondary one via  $\alpha$ -, n-, and p-captures on neutron-rich seeds such as  $^{22}\text{Ne}$  and  $^{23}\text{Na}$  (Roederer & Lawler 2021b). In the Milky Way it behaves mainly as a secondary element, with metallicity-dependent trends (Kobayashi et al. 2020), and its yield further depends on stellar population and star formation history across environments.

Hasselquist et al. (2024) investigated aluminium abundances in the Milky Way and its satellite galaxies using a two-process model, in which abundances are interpreted as the sum of a prompt component from core-collapse supernovae and a delayed contribution from Type Ia supernovae. They found that  $[Al/Mg]$  residuals in the Large Magellanic Cloud and Sagittarius dwarf spheroidal galaxy correlate more strongly with  $[(C+N)/H]$  than with  $[Mg/H]$ , suggesting that C and N act as more direct tracers of the nucleosynthetic pathways responsible for aluminium.

A key result of their study is that when the two-process model is calibrated on Milky Way stars, it systematically overpredicts aluminium abundances in satellite galaxies by 0.1–0.3 dex, particularly at higher metallicities. This mismatch implies that aluminium enrichment in dwarf galaxies follows a different chemical evolution than in the Milky Way. When the model is recalibrated using Sagittarius stars, the resulting dwarf-galaxy-trained model successfully reproduces the aluminium abundances across a wide range of satellites. This demonstrates that while aluminium is a powerful tracer, its interpretation depends sensitively on the galactic environment, and that models must be tailored accordingly.

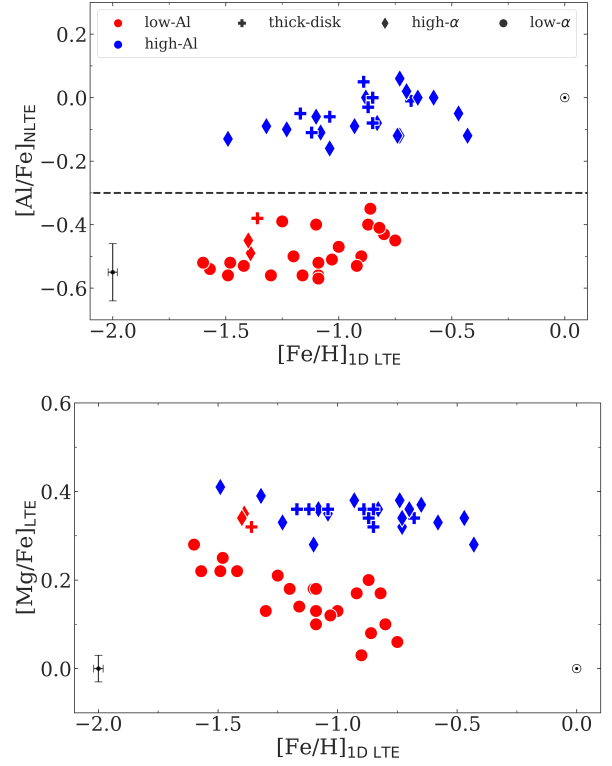


**Fig. 4.** Upper panel:  $[Al/Fe]$  as a function of  $[Fe/H]$  for the stellar sample. The elemental abundances derived under NLTE assumptions for the Al I 3961 Å line. Colour-coded by high-Al and low-Al, with symbols following the (Nissen & Schuster 2010) classification. The thick-disk stars are represented as crosses, high- $\alpha$  stars are shown as diamonds, and low- $\alpha$  stars as circles. Lower panel: Distribution of the stellar sample in the  $[Mg/Fe]_{\text{NLTE}}$  versus  $[Fe/H]_{\text{LTE}}$  according to the low-Al and high-Al classification in this paper and the same symbols as the upper panel.

Together, these considerations show both the power and the limitations of aluminium as a chemical tag. While aluminium abundances provide a robust empirical discriminator between in-situ and accreted populations, their nucleosynthetic interpretation is complex and requires careful consideration of stellar yields, NLTE effects, and environmental dependence.

### 7.3. Kinematic selections

The energies, radial action angle, and angular momenta of the stars in our sample were calculated using the *galpy* package (Bovy 2015). Distances (distance\_gspphot) and proper motions were adopted from *Gaia* Data Release 3 (Gaia Collaboration et al. 2016, 2023), while radial velocities were taken from Nissen & Schuster (2010, 2011). We assumed the *MWPotential2014* Galactic potential model (Bovy 2015) and applied the actionAngleStaeckel approximation (Binney 2012; Bovy & Rix 2013), using a delta value of 0.4. The typical uncertainties in the input parameters are 0.7 pc in distance,  $0.03 \text{ mas yr}^{-1}$  in proper motion, and  $0.3 \text{ km s}^{-1}$  in radial velocity. Propagating these uncertainties through a Monte Carlo analysis, as described by Feuillet et al. (2020), yields typical uncertainties of  $0.12 \times 10^3 \text{ kpc km s}^{-1}$  in angular momentum and  $0.28 \times 10^4 \text{ km}^2 \text{ s}^{-2}$  in orbital energy, and  $2 (\text{kpc km s}^{-1})^{1/2}$  in  $\sqrt{J_R}$ .

The distribution of stars in the  $\sqrt{J_R}$ – $L_Z$  space is shown in Fig. 5. The selection proposed by Feuillet et al. (2021), which

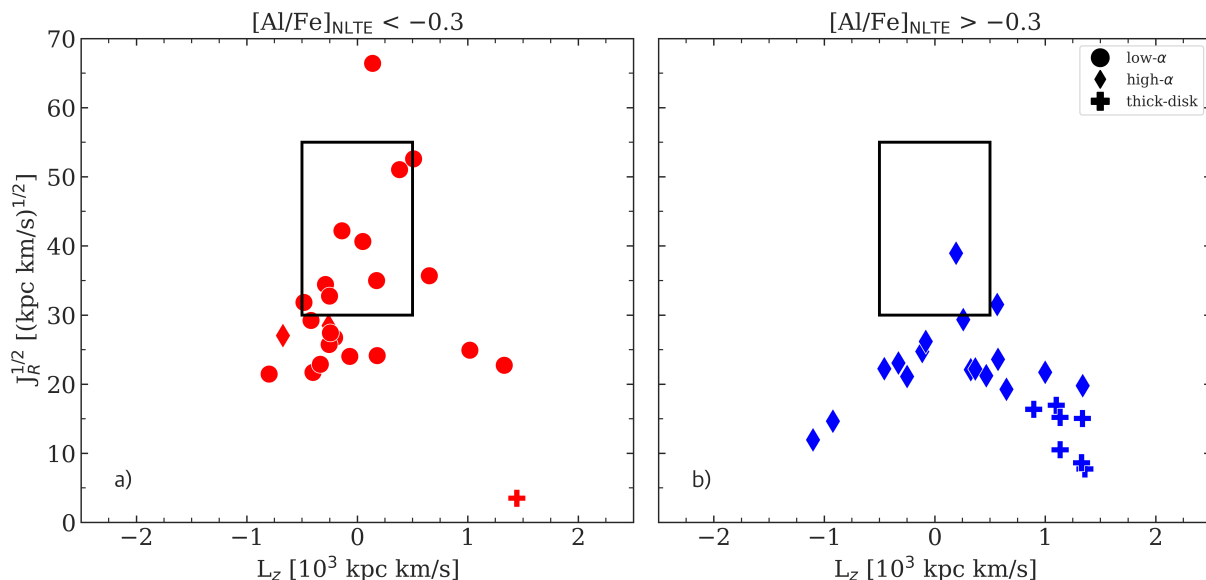


**Fig. 5.** The two panels show  $\sqrt{J_R}$  versus angular momentum,  $L_z$ , for the stellar sample. Panel a) shows the low-Al stars. Panel b) displays the high-Al stars. The low- $\alpha$  are displayed as filled circles, high- $\alpha$  diamonds, and the thick-disk stars are displayed as crosses in both panels. The black box represents the Feuillet et al. (2022) selection scheme for the *Gaia*-Sausage-Enceladus.

has been described by Carrillo et al. (2024) as one of the purest kinematic criteria for identifying the *Gaia*-Sausage-Enceladus population, is confirmed to have a high degree of purity when applied to our low- $\alpha$  and low-aluminium stars. However, we also find that this selection misses a high fraction (>50%) of low-Al stars at smaller  $\sqrt{J_R}$  values, deeper in the Galactic potential, where the distinction between accreted and in-situ stars becomes more ambiguous. This difficulty is exacerbated when adopting more realistic Galactic potentials that account for the influence of non-axisymmetric structures, such as the bar, which further complicate the kinematic separation of halo populations (Dilamore & Sanders 2025).

Our results suggest that a refined kinematic selection may be possible when combined with aluminium abundances. Specifically, stars with  $[Al/Fe] < -0.3$  are highly likely to belong to the *Gaia*-Sausage-Enceladus population, even if their kinematics fall outside the strict boundaries of proposed criteria. Within our dataset, low-aluminium stars are to be found in the region  $-1000 < L_z < 500 \text{ kpc km s}^{-1}$  and  $20 < \sqrt{J_R} < 55 \text{ kpc km s}^{-1/2}$  when aluminium is available. This suggests that extending existing kinematic selections to include stars with lower  $J_R$  values may improve completeness without significantly sacrificing purity.

We emphasise, however, that abundance-based selections should be calibrated on the data in the case of a survey, since the precise threshold in  $[Al/Fe]$  may vary between surveys depending on the adopted analysis and systematic differences in stellar parameters, see Sect. 7.4.

#### 7.4. $[Mg/Mn]$ vs. $[Al/Fe]$ using the *Al I* resonance lines

An important step is to place our  $[Al/Fe]$  measurements in context with other elemental abundances and independent datasets. In Fig. 6 we show our sample of the Nissen & Schuster stars in the  $[Mg/Mn]$  versus  $[Al/Fe]$  plane. This diagnostic has recently been demonstrated to be a powerful tool to disentangle accreted from in-situ populations, as magnesium and manganese probe

distinct nucleosynthetic channels while aluminium provides an additional constraint Hawkins et al. (2015). Our sample fall consistently into the expected location of high- and low- $\alpha$  populations, supporting the robustness of the Al-based classification.

When comparing our aluminium abundances with those derived from APOGEE, which are based on the H-band *Al I* lines near  $1.5 \mu\text{m}$ , we find a systematic offset of  $\sim +0.25$  dex. Most of this offset can be explained by the NLTE correction of the *Al I* H-band lines. As discussed in Section 4.2.1 of Feltzing & Feuillet (2023), the NLTE corrections for the *Al I* lines in the H-band are expected to be about  $-0.2$  dex in  $[Al/H]$  for a giant star such as Arcturus, based on the calculations by Nordlander & Lind (2017). Since our APOGEE subsample consists exclusively of giants, we adopted this value as a representative correction and applied it to the APOGEE  $[Al/Fe]$  abundances. We corrected the  $[Al/Fe]$  (by  $-0.2$  dex), as Feltzing & Feuillet (2023) argued that NLTE effects on  $[Fe/H]$  should be negligible for these stars.

For the magnesium and manganese corrections, Feltzing & Feuillet (2023) discuss that, for giant stars, the NLTE correction for the APOGEE lines corresponds to about  $-0.35$  dex in  $[Mg/Mn]$ . We verified this value in the MPIA web interface<sup>3</sup>, which indeed provides consistent results for the H-band lines. For dwarf stars, we considered the corrections derived from the optical lines for Mg and Mn, as adopted in Nissen & Schuster (2010). In this case, the NLTE corrections are negligible ( $\sim 0.0$  dex) for  $[Mg/Fe]$  and about  $+0.10$  dex for  $[Mn/Fe]$ . Taken together, this implies a NLTE correction of roughly  $-0.10$  dex in  $[Mg/Mn]$  for dwarf stars,  $\sim 0.25$  dex smaller than the value found for giants. Since these are very rough estimates and we are not focusing on Mg and Mn lines, we chose not to apply these corrections to the y-axis of Fig. 6, and instead present only  $[Mg/Mn]_{\text{LTE}}$ . A more complete treatment of NLTE effects, including  $\langle 3D \rangle$  NLTE corrections for Mg, Mn, Al, and Fe across a theoretical grid, is underway and will be presented in Erandes et al. (in prep.).

<sup>3</sup> [https://nlte.mpia.de/gui-siuAC\\_secE.php](https://nlte.mpia.de/gui-siuAC_secE.php)



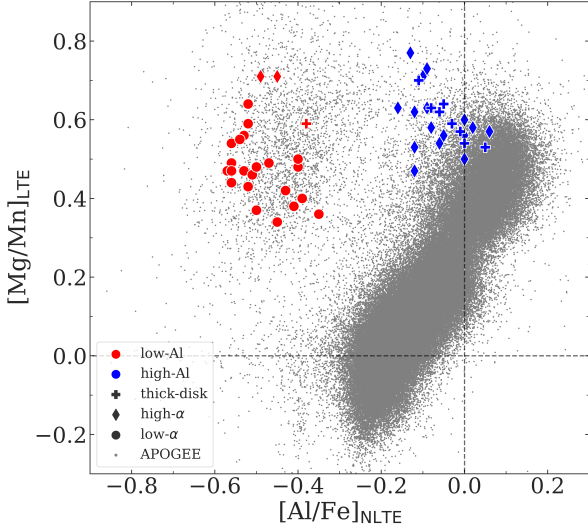


**Fig. 6.** Distribution of stars in the [Mg/Mn] versus [Al/Fe] parameter space. The background grey points show APOGEE DR17 giant stars ( $\log g < 3.0$ ) for reference. Our sample is overplotted with the same symbols as in Fig. 4.

### 7.5. Comments on individual stars

In the new classification of low-Al and high-Al, some stars showed discrepancies from the Nissen & Schuster classification of low- and high- $\alpha$  stars. The stars BD+07 4841, CD-33 3337, and G 24-25 exhibit unexpected aluminium abundances considering their previous classification, as shown in Fig. 4.

- BD+07 4841: This star was classified as a high- $\alpha$  star by Nissen & Schuster (2010). However, its aluminium abundance does not follow the typical pattern of high- $\alpha$  stars, as also evident from the line fitting shown in Fig. 7.
- CD-33 3337: This star was classified by Nissen & Schuster (2010) as a thick disk star based on its kinematics. However, its aluminium abundance differs significantly from that expected for thick disk stars, as seen in the [Al/Fe] vs. [Fe/H] plot in Fig. 4. Additionally, its [Mg/Mn] and [Al/Fe] ratios correspond to a low-aluminium disk population (Feltzing & Feuillet 2023) as shown in Fig. 6. The derived abundances are confirmed by the spectral line fitting in Fig. 7. In the  $En-L_z$  diagram, the star still lies within the disk region.
- G 24-25: This star is classified as a high- $\alpha$  star by Nissen & Schuster (2010), and in *Simbad*, it is identified as both a spectroscopic binary (SB1) and a CEMP-s, features that are evident in its spectrum shown in Fig. 1.

The fact that these stars have  $[Fe/H] \sim -1.5$ , a region where it is hard to distinguish these two populations in the  $[\alpha/Fe]$  plot, can help explain the difference in classification for BD+07 4841. This could also be the case for G 24-25, or it may simply be the fact that CEMP-s stars have unusual abundance patterns. This may lead to a misplacement of this star in a population. As the categorisation based on kinematics and [Al/Fe] abundance is at odds for CD-33 3337, further investigation is needed to determine the origins of this star.

## 8. Conclusions

In this work, we have derived aluminium abundances for a carefully selected subsample of halo stars from the Nissen &

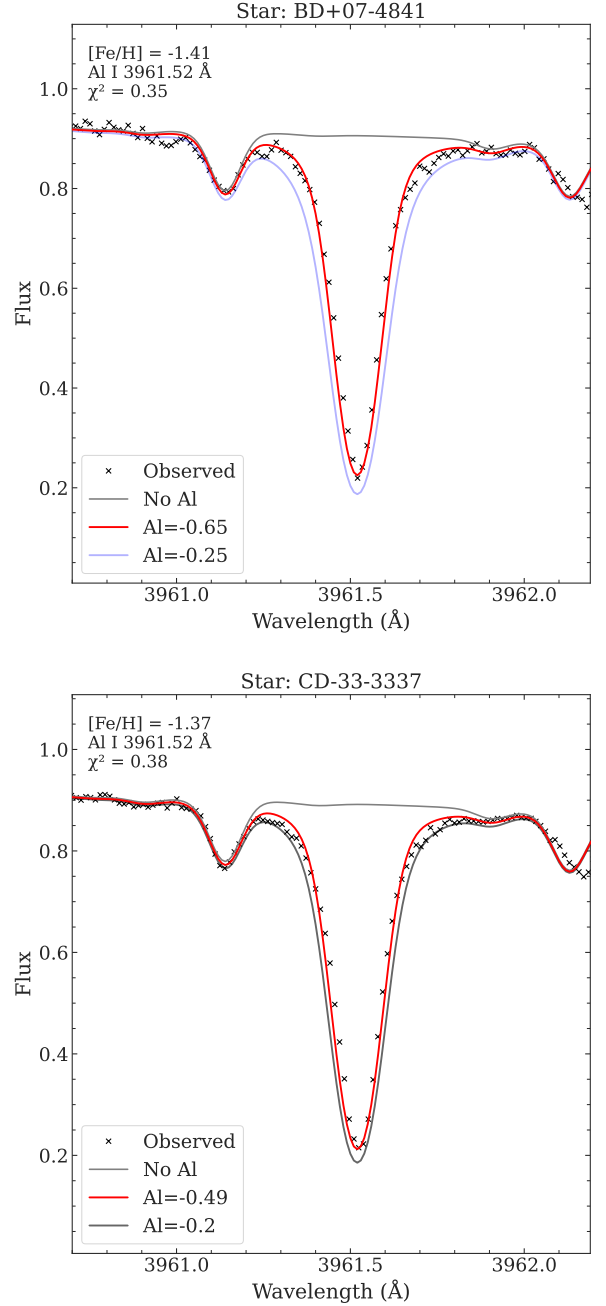


**Fig. 7.** Line profile fits for the Al I LTE at the 3961 Å line in two stars that show atypical abundance patterns for their assigned class in Nissen & Schuster (2011). Panel a) BD+07 4841, a high- $\alpha$  star with low [Al/Fe], and panel b) CD-33-3337, a thick-disk (TD) star with unusually low [Al/Fe] compared to typical TD trends. Observed spectra are shown in black, synthetic fits in colour for different [Al/Fe] values.

Schuster dataset, combining new VLT/UVES observations with archival spectra. Elemental abundances were derived from the Al I 3944 and 3961 Å resonance lines using line-profile fitting under both LTE and NLTE assumptions. Our main conclusions are as follows:

First, the separation between accreted and in-situ halo populations is clear in aluminium abundances, even down to low  $[Fe/H] \approx -1.5$ . This distinction is already present in LTE but becomes significantly enhanced once NLTE corrections are applied. We propose a classification threshold at  $[Al/Fe] = -0.3$  to

distinguish between high- and low-aluminium stars, which correlates to in situ and accreted stars, respectively.

Second, aluminium abundances provide an effective chemical diagnostic that complements  $\alpha$ -element abundances. In particular, aluminium offers a cleaner separation than  $[\alpha/\text{Fe}]$  at low metallicities, thereby improving upon the classical Nissen & Schuster classification, especially when NLTE corrections are applied.

Third, while aluminium is a powerful empirical discriminator, its nucleosynthetic interpretation is complex. Aluminium can behave as either a primary or secondary element, depending on the underlying stellar populations and chemical enrichment history (Woosley & Weaver 1995; Kobayashi et al. 2020). Comparisons with dwarf galaxies confirm that chemical evolution models calibrated on the Milky Way systematically overpredict aluminium in external systems, underlining the need for environment-specific yields and models (Hasselquist et al. 2024).

Finally, we emphasise the importance of combining elemental abundances with kinematic information. While some kinematic selection can provide high-purity samples of accreted stars, they may miss parts of the population, especially at low energies, which can cause biases in the selected samples. Aluminium abundances can serve as an independent and complementary way to probe, providing a robust means to distinguish between accreted and in-situ halo populations in the metal-poor regime. And it has even been used to investigate internal variations in star formation history within the *Gaia*-Sausage-Enceladus progenitor galaxy, as shown in Skúladóttir et al. (2025).

Overall, our results confirm that aluminium abundances, when measured with high-quality spectra and analysed with NLTE corrections, are a powerful tool to trace the origin of halo stars. They provide a reliable chemical tag for accreted populations, opening new possibilities for disentangling the complex assembly history of the Milky Way.

## Acknowledgements

H.E., S.F., and D.F. were supported by a project grant from the Knut and Alice Wallenberg Foundation (KAW 2020.0061 Galactic Time Machine, PI Feltzing). H.E. is supported by foundations managed by The Royal Swedish Academy of Sciences. and supported by The Royal Physiographic Society in Lund (reference 162011). This project was supported by funds from the Crafoord Foundation (reference 20230890). D.F. acknowledges funding from the Swedish Research Council grant 2022-03274. Á.S. acknowledges funding from the European Research Council (ERC) under the European Union's Horizon 2020 research and innovation programme (grant agreement No. 101117455).

## References

Abbott, B. P., Abbott, R., Abbott, T. D., et al. 2017, *ApJ*, 851, L35  
 Alvarez, R. & Plez, B. 1998, *A&A*, 330, 1109  
 Amarsi, A. M., Liljegren, S., & Nissen, P. E. 2022, *A&A*, 668, A68  
 Amarsi, A. M., Nissen, P. E., Asplund, M., Lind, K., & Barklem, P. S. 2019, *A&A*, 622, L4  
 Barklem, P. S., Piskunov, N., & O'Mara, B. J. 2000, *Astron. and Astrophys. Suppl. Ser.*, 142, 467, (BPM)  
 Belokurov, V., Erkal, D., Evans, N. W., Koposov, S. E., & Deason, A. J. 2018, *MNRAS*, 478, 611  
 Bensby, T., Feltzing, S., & Lundström, I. 2004, *A&A*, 415, 155  
 Binney, J. 2012, *MNRAS*, 426, 1324  
 Bovy, J. 2015, *ApJS*, 216, 29  
 Bovy, J. & Rix, H.-W. 2013, *ApJ*, 779, 115

Brown, J. M. & Evenson, K. M. 1999, *Phys. Rev. A*, 60, 956  
 Buder, S., Sharma, S., Kos, J., et al. 2021, *MNRAS*, 506, 150  
 Carrillo, A., Deason, A. J., Fattahi, A., Callingham, T. M., & Grand, R. J. J. 2024, *MNRAS*, 527, 2165  
 Dekker, H., D'Odorico, S., Kaufer, A., Delabre, B., & Kotzlowski, H. 2000, in *Society of Photo-Optical Instrumentation Engineers (SPIE) Conference Series*, Vol. 4008, *Optical and IR Telescope Instrumentation and Detectors*, ed. M. Iye & A. F. Moorwood, 534–545  
 Dillamore, A. M. & Sanders, J. L. 2025, *arXiv e-prints*, arXiv:2506.09117  
 Edlén, B. & Risberg, P. 1956, *Ark. Fys.*, 10, 553  
 Epstein, C. R., Johnson, J. A., Dong, S., et al. 2010, *The Astrophysical Journal*, 709, 447  
 Eriksson, K. & Isberg, H. 1963, *Ark. Fys.*, 23, 527  
 Erandes, H., Barbuy, B., Friaça, A. C. S., et al. 2020, *A&A*, 640, A89  
 Erandes, H., Feuillet, D., Feltzing, S., & Skúladóttir, Á. 2024, *A&A*, 691, A333  
 Ezzeddine, R., Merle, T., Plez, B., et al. 2018, *A&A*, 618, A141  
 Feltzing, S. & Feuillet, D. 2023, *ApJ*, 953, 143  
 Feuillet, D. K., Feltzing, S., Sahlholdt, C., & Bensby, T. 2022, *ApJ*, 934, 21  
 Feuillet, D. K., Feltzing, S., Sahlholdt, C. L., & Casagrande, L. 2020, *MNRAS*, 497, 109  
 Feuillet, D. K., Sahlholdt, C. L., Feltzing, S., & Casagrande, L. 2021, *MNRAS*, 508, 1489  
 Freuding, W., Romaniello, M., Bramich, D. M., et al. 2013, *A&A*, 559, A96  
 Gaia Collaboration, Prusti, T., de Bruijne, J. H. J., et al. 2016, *A&A*, 595, A1  
 Gaia Collaboration, Vallenari, A., Brown, A. G. A., et al. 2023, *A&A*, 674, A1  
 Gerber, J. M., Magg, E., Plez, B., et al. 2023, *A&A*, 669, A43  
 Hasselquist, S., Hayes, C. R., Griffith, E. J., et al. 2024, *ApJ*, 974, 227  
 Hasselquist, S., Hayes, C. R., Lian, J., et al. 2021, *ApJ*, 923, 172  
 Hawkins, K., Jofré, P., Masseron, T., & Gilmore, G. 2015, *Monthly Notices of the Royal Astronomical Society*, 453, 758  
 Kobayashi, C., Karakas, A. I., & Lugaro, M. 2020, *ApJ*, 900, 179  
 Koutsouridou, I., Skúladóttir, Á., & Salvadori, S. 2025, *A&A*, 699, A32  
 Limberg, G., Souza, S. O., Pérez-Villegas, A., et al. 2022, *ApJ*, 935, 109  
 Lindegren, L. & Feltzing, S. 2013, *A&A*, 553, A94  
 Naidu, R. P., Ji, A. P., Conroy, C., et al. 2022, *ApJ*, 926, L36  
 Nissen, P. E., Amarsi, A. M., Skúladóttir, Á., & Schuster, W. J. 2024, *A&A*, 682, A116  
 Nissen, P. E. & Schuster, W. J. 2010, *A&A*, 511, L10  
 Nissen, P. E. & Schuster, W. J. 2011, *A&A*, 530, A15  
 Nordlander, T. & Lind, K. 2017, *A&A*, 607, A75  
 Plez, B. 2012, *Turbospectrum: Code for spectral synthesis*, *Astrophysics Source Code Library*, record ascl:1205.004  
 Roederer, I. U. & Lawler, J. E. 2021a, *ApJ*, 912, 119  
 Roederer, I. U. & Lawler, J. E. 2021b, *ApJ*, 912, 119  
 Skúladóttir, Á., Erandes, H., Feuillet, D. K., et al. 2025, *ApJ*, 986, L21  
 Smith, W. H. & Liszt, H. S. 1971, *Journal of the Optical Society of America* (1917-1983), 61, 938, (SLa)  
 Woosley, S. E. & Weaver, T. A. 1995, *ApJS*, 101, 181  
 Zhan-Kui, J., Lundberg, H., & Svanberg, S. 1982, *Physics Letters A*, 92, 27

## Appendix A: Radial velocity table

We present the radial velocities derived following the methodology in Section 2. We note that HD 111980 is a known spectroscopic binary, SB1, as listed in Simbad.

## Appendix B: NLTE corrections

We present the NLTE corrections applied to the Al I 3961 Å line for this sample as a function of  $[\text{Fe}/\text{H}]_{\text{LTE}}$ ,  $T_{\text{eff}}$ , and  $\log g$ . As seen in Fig. B.1, the corrections are  $\sim +0.2$  dex in [Al/Fe] for all stars in our sample. We do not observe any significant dependency with stellar parameters.

**Table A.1.** Measured radial velocities for the stellar sample, corrected to the heliocentric rest frame. The table also lists the number of OBs co-added per star. Stars with an asterisk ‘\*’ are known spectroscopic binaries. These velocities were used to correct each exposure before coaddition and abundance analysis.

Star	OBs	Radial velocity [kms <sup>-1</sup> ]
BD+00 2058A	1	+83.28
BD+02 2541	2	−153.80
BD+06 2932	1	+144.31
BD+07 4841	1	+234.19
BD+11 2369	1	−28.37
BD+11 4725	1	+197.03
BD+18 3423	1	+240.81
BD-01 306	1	−28.91
BD-03 56	1	+28.19
BD-06 855	1	−295.46
BD-08 4501	1	−84.58
CD-33 3337	1	−74.30
CD-43 6810	1	−166.23
CD-57 1633	4	−261.02
CD-61 282	1	−220.80
G 24-25	1	+303.93
G 63-26	4	−58.04
G 75-31	1	−58.00
HD 103723	1	−168.80
HD 105004	1	−122.12
HD 106516	2	−12.13
HD 111980*	3	−150.02
HD 113679	1	−157.84
HD 120559	1	−17.70
HD 121004	1	−245.07
HD 132475	4	−176.66
HD 148816	1	+47.73
HD 159482	2	+135.28
HD 163810	2	−185.17
HD 177095	1	−90.72
HD 179626	1	+64.74
HD 189558	1	+12.34
HD 193901	2	+171.19
HD 194598	3	+247.02
HD 199289	1	+5.94
HD 205650	1	+102.38
HD 219617	2	−13.91
HD 22879	1	−120.49
HD 284248	2	−339.08
HD 298986	1	−198.63
HD 3567	2	+47.43
HD 51754	1	+94.05
HD 59392	2	−268.51
HD 76932	1	−120.18
Wolf 615	2	−170.67
Archival spectra		
CD-45-3283	1	−309.36
G 46-31	3	−227.19
G 87-13	1	−206.46
G 98-53	1	−144.08
G 114-42	2	+86.300
G 161-73	1	−121.04
G 53-41	3	−88.30
G 119-64	1	+196.10
G 05-36	1	+9.88
G 188-22	1	+94.77
HD 25704	9	−56.130

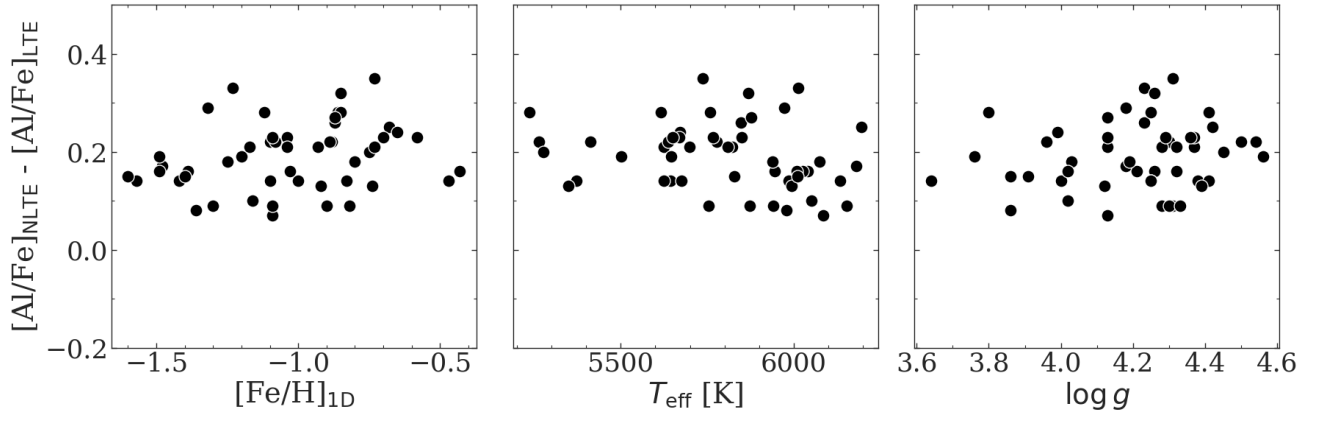


**Fig. B.1.** NLTE corrections for the Al I 3961 Å line as a function of stellar parameters. The three panels show the NLTE correction as a function of  $[Fe/H]$ ,  $T_{eff}$  and  $\log g$ , respectively.